Research Square

Preprints are preliminary reports that have not undergone peer review.
They should not be considered conclusive, used to inform clinical practice,
or referenced by the media as validated information.

Non-invasive Detection of Neuronal Electrical Activity in the Knee Joint Using Quantum Sensing MRI

Anmol Monga

anmol.monga@nyulangone.org

NYU Grossman School of Medicine

Hector L. de Moura

NYU Grossman School of Medicine

Jonathan Samuels

NYU Grossman School of Medicine

Yongxian Qian

NYU Grossman School of Medicine

Ravinder Regatte

NYU Grossman School of Medicine

Article

Keywords: Osteoarthritis, Knee joint, Neuronal activity, Magnetic resonance imaging (MRI), Free induction decay (FID), Quantum sensing MRI

Posted Date: November 3rd, 2026

DOI: https://doi.org/10.21203/rs.3.rs-11327314/v1

License: This work is licensed under a Creative Commons Attribution 4.0 International License.
Read Full License

Additional Declarations: Competing interest reported. YQ is the inventor of U.S. Patent Application No. 63/467,482, titled “Systems and methods for non-invasive detection of neuronal firings in humans via quantum-sensing magnetic resonance imaging,” filed on May 18, 2023. The intellectual property is owned by New York University. All other authors (AM, HLM, JS, and RR) declare no conflicts of interest.

Non-invasive Detection of Neuronal Electrical Activity in the Knee Joint Using Quantum Sensing MRI

[1]Center for Biomedical Imaging, Department of Radiology, NYU Grossman School of Medicine, New York, New York, USA

[2]Department of Medicine, NYU Grossman School of Medicine, New York, New York, USA

Author Information

Anmol Monga, MS[1]; Hector L. De Moura, PhD[1]; Jonathan Samuels, MD[2]; Yongxian Qian, PhD[1]; Ravinder Regatte, PhD[1]

Anmol Monga MS, anmol.monga@nyulangone.org, ORCID 0009-0001-5248-3126

Hector L. de Moura PhD[1], hector.lisedemoura@nyulangone.org, ORCID 0000-0002-6620-9814

Jonathan Samuels MD[2], jonathan.samuels@nyulangone.org, ORCID 0000-0002-1513-770X

Yongxian Qian, PhD[1], yongxian.qian@nyulangone.org, ORCID 0000-0002-9931-7790

Ravinder Regatte, PhD[1], ravinder.regatte@nyulangone.org, ORCID 0000-0002-4607-7682

Corresponding Author:

Anmol Monga, MS
Center for Biomedical Imaging
NYU Grossman School of Medicine
New York, NY, USA
Email: anmol.monga@nyulangone.org

Running Title: Knee Joint Neuronal Activity via Quantum Sensing MRI

Non-invasive Detection of Neuronal Electrical Activity in the Knee Joint Using Quantum Sensing MRI

Abstract

Noninvasive assessment of neuronal activity in the knee may improve understanding of osteoarthritis (OA)-related pain and joint degeneration. A 3T quantum-sensing based MRI framework was developed to estimate firing-rate-related signal fluctuations from free induction decay (FID) phase measurements, separating water and fat signals for compartment-specific estimates. The approach was evaluated in agar-gel phantoms, simulations, and six healthy volunteers and six participants with early knee OA, at rest and during repeated ankle flexion. No firing events were detected in the phantom. Simulation performance improved with signal-to-noise ratio, reaching R^2=0.99 at SNR=250. In vivo, water-derived estimates correlated negatively with $T_{1\rho}$ relaxation times (cartilage, r = -0.86 to -0.58; meniscus, r = -0.78 to -0.73). Fat-derived estimates differentiated OA participants from healthy volunteers (d = 3.96-4.89; $p<0.05$), correlated positively with $T_{1\rho}$ (cartilage r = 0.59-0.70; meniscus r = 0.70-0.71) and showed moderate exploratory associations with WOMAC scores (r = 0.43-0.55). Repeatability was higher during ankle flexion than at rest. These findings support the technical feasibility of compartment-specific FID phase analysis in the knee. Larger studies with physiological-noise control and independent biological validation are required to determine whether these MRI-derived measures specifically reflect peripheral neuronal activity and have clinical utility in OA.

Keywords: Osteoarthritis; Knee joint; Neuronal activity; Magnetic resonance imaging (MRI); Free induction decay (FID); Quantum sensing MRI.

Introduction

The knee is a complex load-bearing joint whose function depends on the coordinated interaction between bones, cartilage, ligaments, menisci, synovium, and surrounding connective tissues. Its sensory and autonomic innervation regulates nociception, proprioception, reflex activity, and local vascular function.[1–8] Osteoarthritis (OA) is a whole-joint disease involving interrelated mechanical, cellular, inflammatory, and biochemical changes across these tissues.[9–19] Although cartilage degeneration is a defining feature of OA, cartilage is aneural; OA pain is thought to arise mainly from innervated structures, including synovium, subchondral bone, menisci, ligaments, and

infrapatellar fat pad. Neural remodeling, sensitization, and inflammatory mediators may contribute to pain and disease progression.[20–26]

Despite its central role in OA, direct measurement of neuronal activity within the knee joint remains limited. Invasive electrophysiology in animal models provides high-fidelity recordings but lacks translational applicability.[26] In humans, microneurography is minimally invasive but technically challenging, with limited spatial specificity and sampling.[27] Noninvasive techniques such as electroencephalography rely on large-scale neuronal synchrony and are not suited for detecting sparse peripheral nerve activity,[28] while electromyography reflects muscle activation rather than sensory nerve firing.[29,30]

To address this limitation, we evaluate a quantum sensing MRI approach for noninvasive assessment of neuronal activity in the knee joint. In MRI, nuclear spins of proton provide an ensemble of quantum sensors. The local magnetic-field perturbations can alter the Larmor precession frequency of proton and accumulate as phase changes in free induction decay (FID) signal. This mechanism may enable detection of weak magnetic-field perturbations associated with neuronal currents through analysis of phase variations in free induction decay signals.[31] By leveraging the spatial sensitivity of multi-channel receiver coils, this framework enables localization of neuronal activity and provides a potential imaging-based biomarker for peripheral neural dynamics in knee OA.

Results

Figure 1 summarizes the conceptual basis of the FID phase-based analysis, whereas **Figure 2** illustrates the practical processing workflow. Briefly, multi-channel FID signals were separated into water- and fat-dominant components in the frequency domain. Instantaneous Phase variations in each separate FID were then used to derive the apparent neuronal firing field over time. Peaks identified were counted within the analyzed acquisition window, and firing rate (FR) was defined as the number of detected peaks per second. FR was calculated separately for each coil element and repetition, and the median value across 64 repetitions was used for subsequent analyses. In the experiment, Water- and fat-derived firing-rate measures were calculated separately under rest and flexion conditions. **Rest** denotes acquisition with the ankle maintained at rest. **Flexion** denotes acquisition during repeated ankle plantar flexion while the knee

remained stationary. The FR values are evaluated based on their association with OA status, $T_{1\rho}$ values (cartilage, meniscus, and its subregions), and WOMAC scores. **Figure 3A** shows the anatomical subdivision of cartilage and meniscal regions used for regional analysis, and **Figure 3B** presents representative $T_{1\rho}$ maps. **Figure 3C** illustrates the two FID acquisition conditions: rest and repeated ankle flexion. FID signals acquired under each condition were processed to estimate firing rate (FR). Full acquisition and processing details are provided in the Methods.

Noise Sensitivity and Simulation. To evaluate non-biological noise, FR was measured in a phantom containing 3%, 5%, and 7% agar gel and rubber. Across all channels and three repetitions, FR was 0 Hz, with only sparse, thin spikes visible in the neuronal firing field (**Figure 4C, 4G, 4K**; firing rates in **4D, 4H, 4L**). Simulations assessed noise effects on neuronal firing estimation using six Gaussian peaks with decreasing amplitude and alternating polarity (**Figure 5A)**. As SNR increased, estimation accuracy improved (**Figure 5C-5F**). At SNR = 250, R^2 = 0.99, slope ≈ 0.99, and CV = 13%, while lower SNR (50, 100, 150) showed progressively larger errors (CV = 170%, 66%, 40%). Smaller peaks (<10 μT) were particularly susceptible to noise (**Figure 5B)**, with T_2* decay and firing duration influencing reliability.

Association with OA status. **Figure 6A** illustrates variation in $T_{1\rho}$ for cartilage (all subregions) and meniscus (all subregions) between the OA-affected cohort and healthy controls. In **Figure 6B**, OA patients exhibited lower water- and higher fat-signal FR (averaged across channels) than controls, with no consistent differences between rest and flexion. The effect size for fat-signal FR is larger than for cartilage. Water- and fat-signal FR values show differences between OA and healthy control, but the differences are more pronounced for Fat-signal FR values. **Table 1** summarizes median FR values for water and fat FIDs across channels in left/right and rest/flexion. For water FID, FR was consistently lower in OA compared to healthy controls, particularly in K4–K15 (up to −33.7%), whereas fat FID showed higher FR in OA (up to +64.4%). No significant differences were observed between rest and flexion.

Association with $T_{1\rho}$. In **Figure 6C**, the water-signal FR averaged across channels is negatively correlated with $T_{1\rho}$ value for cartilage (Water Component: r = -0.58, p-value=0.039, slope=-1.8) and meniscus (r = -0.78, p-value=0.002, slope=-2.0). In contrast, the fat-signal FR is positively correlated with $T_{1\rho}$ value for cartilage (r = 0.59, p-value = 0.035, slope=5.1) and meniscus (r = 0.70, p-value=0.007, slope-4.9). During Ankle flexion, the cartilage FR (both water and fat FID)

see increase in absolute strength of correlation and slope (r decreases from -0.58 to -0.86 in water FID; increases from 0.59 to 0.70 in fat FID). Visual inspection suggested reduced dispersion around the fitted relationships during flexion; however, this observation requires formal evaluation and may reflect changes in measurement stability or other flexion-related effects. In exploratory channel-specific analyses of FR and sub-regional $T_{1\rho}$, the water-signal FR showed predominantly negative correlations with $T_{1\rho}$ (**Figure S1A-S1C; Figure S2A-S2C)**, strongest in middle coil elements, whereas fat-signal FR exhibited widespread positive correlations (**Figure S1A-S1C**), particularly in the meniscus.

Association with WOMAC. Water-signal FR showed no significant association with WOMAC scores. In contrast, fat-signal FR showed moderate positive correlation with total score ($r = 0.52$, $p = 0.069$; slope = 0.5), function ($r = 0.55$, $p = 0.05$; slope = 0.8), and pain ($r = 0.43$, $p = 0.147$; slope = 2), indicating a closer link between fat FID neuronal activity and OA severity (**Figure 7**).

Repeatability. In three healthy subjects, FR repeatability was evaluated across coil elements K1–K15. For water FID, variability was higher at rest (LOA: +33.4%, −31.2%; ICC = 0.772) than during flexion (LOA: +22.1%, −19.1%; ICC = 0.898), with spatial variation greatest in inferior elements (K1–K5). Fat FID showed lower repeatability (ICC: 0.573–0.602) and higher CV at rest, particularly in central elements (K6–K10). Flexion reduced variability across both water and fat FIDs (**Figure 8**).

Discussion

This study evaluates the feasibility of estimating neuronal firing fields from FID signals and systematically characterizes the impact of noise on the estimation pipeline. Phantom experiments confirmed that the proposed method does not generate spurious neuronal firing, with firing rates consistently 0 Hz despite non-biological noise, indicating robustness to false positives. Simulation results revealed that accurate estimation of neuronal firing amplitude is highly dependent on SNR. At high SNR (~250), the method achieves near-perfect agreement with ground truth ($R^2 \approx 0.995$, lower CV), whereas performance degrades substantially at lower SNR levels. Noise effects were most pronounced for firing events occurring at later points along the T_2* decay curve.

In vivo, firing rate (FR) estimates were more consistent during flexion than at rest, as indicated by narrower limits of agreement, higher ICC, and lower CV. Differences between water- and fat-

derived FR varied by acquisition condition and spatial location across coil elements, rather than showing consistently superior reliability for one signal type. Distinct relationships between FR and tissue properties were observed. Water-signal FR showed predominantly negative correlations with $T_{1\rho}$, suggesting that elevated $T_{1\rho}$, reflecting tissue degeneration, is associated with reduced neuronal firing in water-sensitive compartments. Conversely, fat-signal FR exhibited strong, spatially widespread positive correlations with $T_{1\rho}$, which became more pronounced during flexion. Flexion enhanced both the strength and spatial extent of these correlations, particularly in meniscal and femoral cartilage regions. Given that elevated $T_{1\rho}$ indicates tissue degeneration in OA, the positive association suggests that fat-derived FR may be sensitive to pathological processes in adipose-rich and periarticular tissues, potentially related to inflammatory or metabolic activity.

Consistent with these findings, fat-derived FR showed stronger associations with clinical outcomes, including moderate to strong correlations with WOMAC scores, whereas water-derived FR showed no significant clinical correlation. These observations align with prior evidence of heterogeneous tissue responses in OA: synovial inflammation and cartilage degeneration are linked to local nerve remodeling and reduced neuronal signaling,[32] whereas subchondral bone and periarticular fat pads often exhibit increased innervation and nerve sprouting, contributing to heightened pain sensitivity[26,33]. Overall, our results suggest that compartment-specific neuronal activity can be potentially captured using FID-based FR measurements, with fat-derived signals reflecting nociceptive processes in OA-relevant adipose and marrow-rich regions, while water-derived FR may serve as a localized indicator of tissue degeneration and altered physiological activity. These findings are consistent with established links between altered innervation, tissue degeneration, and pain sensitivity in OA, supporting the utility of this framework for probing functional neurophysiology in the joint environment.

This study has several limitations. The sample size is small, restricting the generalizability of the findings. The current FID signal model is simplistic, and low-pass filtering may remove relevant temporal features of neuronal activity; more advanced methods are needed to separate water and fat components while preserving neuronal signal characteristics. Physiological noise, including motion, blood flow, and chemical shift variations, was not explicitly modeled and may confound neuronal firing estimates. Spatial resolution is limited by the number and geometry of receiver

coils, potentially causing signal averaging across regions; increasing coil elements, optimizing sensitivity profiles, or using single-voxel excitation could improve localization. Future work will address these limitations, focusing on improved modeling and accounting for physiological noise to enhance the reliability and spatial specificity of neuronal firing measurements.

In conclusion, the estimation of neuronal firing from FID signals is feasible but strongly dependent on SNR, signal amplitude, and decay characteristics. Water- and fat-derived FR provide complementary insights into joint physiology. Water-derived FR primarily reflects localized or condition-dependent variations in neuronal activity, whereas fat-derived FR appears more sensitive to structural degeneration and clinical severity in OA, capturing alterations in innervation and nociceptive signaling associated with disease progression. These findings highlight the potential of compartment-specific FID analysis to noninvasively probe neuronal activity in the knee joint.

Methods

Neuronal Firing Mechanism

Neurons, composed of dendrites, a soma (cell body), an axon, and synaptic terminals, transmit electrical and chemical signals throughout the nervous system. Ion channels along the neuronal membrane mediate electrical signaling.[34] Because neurons do not physically contact each other, communication occurs via neurotransmitters at synapses.

Action potentials propagate along axons through sequential activation of voltage-gated sodium (Na^+) channels (Figure 1A). At rest (~−70 mV), neurons maintain high intracellular potassium (K^+) and high extracellular Na^+. When depolarization exceeds ~−55 mV, Na^+ channels open, rapidly depolarizing the membrane to ~+20–30 mV, followed by K^+-mediated repolarization and transient hyperpolarization. Ionic gradients are restored by the Na^+/K^+ ATPase pump (3 Na^+ out, 2 K^+ in). Temporal evolution of action potential is illustrated in Figure 1B. Action potentials typically last approximately 1–2 ms, although their duration and voltage characteristics vary among neuronal types.[34]

At synaptic terminals, action potentials open voltage-gated calcium (Ca^{2+}) channels, triggering neurotransmitter release into the synaptic cleft. Postsynaptic potentials are smaller, longer, and graded; however, their weak and low-frequency magnetic fields are indistinguishable from MRI

background variations (B_0 and B_1 inhomogeneities). Thus, this study focuses on action potential-related signals.

Firing Rate Assessment Using Quantum Sensing MRI

Action potential generates weak magnetic fields (Figure 1A). In MRI's static field (B_0), these produce small perturbations in the hydrogen nuclear spins, but visible variations in the phase of the free induction decay (FID) signal. MRI signals are voxel-averaged, and extracellular current-induced magnetic fields (quadrupolar) are much smaller than intracellular axonal magnetic fields (dipolar) induced by neuronal firing, leaving the axonal firing as the primary contributor to the variation of FID phase.

We model axons as cylinders, with the nodes of Ranvier represented by oppositely directed currents that form a quadrupolar configuration. Intra-axonal fields are calculated using the Biot–Savart law:

$$B(r,t) = \frac{\mu_0\, n\, q\, v\, r}{2} \quad , \; r < a; \; within\; the\; axon \qquad (1)$$

where $B(r)$ is the neuronal magnetic field at the observation point, n is the number of Na^+ ions, q is the total positive charge, v is the ion velocity, a is the axon radius, and r is the distance to the observation point. The field direction follows the right-hand rule.

The sodium ion (Na^+) concentration differs substantially between intra-axonal and extra-axonal compartments, typically ranging from approximately 15 to 150 mM.[34] Neuronal firing is initiated by the influx of a small fraction of Na^+ ions from the extra-axonal to the intra-axonal space, generating a transient depolarizing current. Innervation of the knee joint is predominantly composed of thin, unmyelinated axons (radius: ~0.25–1 μm), which conduct at velocities of approximately 0.5–2 m/s and are primarily associated with slow, chronic pain signaling.[35,36] A smaller population of myelinated axons (radius: ~2.5-5 μm) is also present, conducting at velocities on the order of ~9 m/s and contributing to fast pain transmission, autonomic regulation, and proprioceptive feedback.[36]

Using Eq. (1), the magnetic field generated by neuronal activity is estimated to span a broad range, approximately 0.119 μT to 182 μT, depending on the assumed ionic concentration (small fraction of extra-axonal Na^+ concentration), drift velocity, and axonal radius. In unmyelinated axons, Na^+ propagation occurs over 1–7 ms, whereas in myelinated axons it takes ~1 ms. Within a single

voxel, contributions from multiple simultaneously firing neurons in the same direction sum, producing an aggregated magnetic field detectable in the MRI- FID. Neuronal firing fields can be directly estimated from FID phase changes using the following equations 2–5, with detailed derivations provided in recent work.[31]

$$\varphi(r,t) = \varphi(r,TE) + \gamma \int_{TE}^{t} B_{n,z}(r,\tau)d\tau \quad (2)$$

$$s(t) = \int_{\Delta V} c(r)\rho(r)e^{-t/T_2^*(r)}e^{-j\varphi(r,t)}dr \quad (3)$$

$$\Delta\varphi(t) = phase[s(t+\Delta t)s^*(t)] \quad (4)$$

$$B_{n,z}(t) \approx \frac{\Delta\varphi(t)}{\gamma\Delta t} \quad (5)$$

where γ is the gyromagnetic ratio, $c(r)$ is coil sensitivity, $\rho(r)$ is proton density, $B_{n,z}$ is the z-component of the neuronal field, $s(t)$ is the FID, and φ is the FID phase.

As shown in Eqs. (2) and (3), neuronal firing accumulates in the FID phase. The instantaneous phase change per unit time can be used to estimate neuronal firing during FID acquisition, as described in Eqs. (4) and (5). **Figure 1C** illustrates the algorithmic workflow used to calculate the firing rate.

Model Phantoms and In Vivo Knee Joint Imaging

All model agar gel phantoms and human subjects were scanned on a 3T scanner (MAGNETOM Prisma, Siemens Healthineers AG, Forchheim, Germany) using a vendor-provided 1-Tx/15-Rx knee coil (QED, OH). Human studies were approved by the local Institutional Review Board (IRB) of New York University (NYU) Grossman School of Medicine (New York, NY, USA) and conducted in accordance with applicable guidelines and regulations. Written informed consent was obtained from all study participants.

A three-compartment agar phantom (3%, 5%, and 7%) was gadolinium-doped to achieve a T_1 of ~900 ms and T_2 values of ~44.1, 27.6, and 22.3 ms, respectively. A rubber eraser was included as a short-T_2 reference, simulating tendons and ligaments.

Six healthy volunteers (3 females; mean age 52.1 ± 16 years; BMI 26.9 ± 4.2; no pain; Kellgren–Lawrence [KL] grade 0) and six patients with early knee osteoarthritis (OA) (5 females; mean age 70.8 ± 5 years; BMI 26.3 ± 4.9; KL grades 1–2) were recruited for this feasibility study. OA patients underwent standardized weight-bearing, fixed-flexion posteroanterior knee radiography using the SynaFlexer positioning frame, as previously described.[37] Inclusion criteria: age 40–75 years for all participants; healthy controls required no knee pain, KL 0, and normal MRI; OA patients required frequent knee pain, KL 1–2 in the index knee, and ≤1 contralaterally. Exclusion criteria: other joint diseases, recent corticosteroid injections (<3 months), prior knee surgery or trauma, planned/prior knee replacement, MRI contraindications, and conditions including avascular necrosis, Paget's disease, Wilson's disease, gout, pregnancy, or major comorbidities (e.g., diabetes, cancer, heart failure, chronic infections).

Imaging Protocol

A product-sequence FID was acquired in the knee using a 0.2 ms RF pulse, which produced a 90° flip angle, followed by signal evolution with TR = 1500 ms. Data were acquired over 64 repetitions, each recording 819 ms of FID (0.2 ms sampling; 2048 points). Signals from all coil elements and repetitions were stored separately, and coil sensitivity maps enabled spatial localization. Total acquisition time was ~1 min 36 s. Two FIDs were acquired per subject: one at rest and one during repeated ankle flexion to induce cyclic loading while keeping the knee stationary. Knee positioning was standardized to center the cartilage within the coil. To account for laterality, six left knees (3 healthy, 3 OA) and six right knees (3 healthy, 3 OA) were scanned. Four T1ρ-weighted images were acquired using spin-lock preparation (TSL = 0.5, 3.8, 9.8, 21.8 ms; 500 Hz). A 3D sagittal dataset (0.8 × 0.8 mm², 3 mm slice, 160 mm FOV) was obtained in 1 min 29 s per TSL. Monoexponential fitting generated T1ρ maps.[38] Coil sensitivity maps derived from k-space were matched across acquisitions and used for FID localization; fixed coil geometry allows reuse across subjects. Acquisition details are summarized in **Table 2**.

Data post-processing

Spatial Localization of Nerve Firings. The spatial origin of the FID signal was determined from the physical positions of individual coil elements, using $T_{1\rho}$-weighted images acquired at TSL = 0.5 ms for anatomical reference. Consistent FOV positioning and shim settings were maintained between imaging and FID acquisitions. Coil-resolved $T_{1\rho}$ images were generated for each element,

but limited contrast made direct identification of FID sources challenging. To improve localization, coil sensitivity maps were estimated using the ESPIRiT algorithm,[39] with each element assigned both a physical and processing-based identifier. Physical coil IDs were matched between $T_{1\rho}$ imaging and FID acquisitions. **Figure S3** shows coil-resolved $T_{1\rho}$ images and corresponding sensitivity maps in axial, coronal, and sagittal views. Using these maps, a nearest-neighbor clustering approach (**Figure S4**) estimated the center of each coil's sensitivity region: K1–K5 localized to the inferior region (proximal tibia/fibula), K6–K10 to the middle region (adjacent to cartilage), and K11–K15 to the superior region. Elements K1, K2, K6, K7, K11, and K12 were primarily posterior, with the remainder anterior. In Eqs. (2)–(5), the FID is assumed to arise solely from independent water protons, neglecting contributions from fat-associated protons. Fat protons resonate at slightly shifted frequencies relative to water, introducing additional phase shifts that could be misinterpreted as neuronal firing. Therefore, FID contributions from water and fat must be separated before estimating neuronal activity.

Water/Fat Separation. The FID spectrum exhibited two dominant lobes corresponding to water and fat. These were separated using a low-pass Gaussian filter, with the frequency-domain representation provided in Eq. (6).

$$G(f) = \frac{1}{\sqrt{2\pi}\sigma} e^{-(f^2)/2\sigma^2} \qquad (6)$$

In Eq. (6), $G(f)$ represents the frequency response of a Gaussian filter centered at $f = 0$, with width controlled by the parameter σ. σ is determined algorithmically by locating the minimum between the fat and water peaks in the FID spectrum, selecting it such that $G(f)$ at this minimum is one-tenth of its maximum. To isolate water, the FID centered at the water peak is passed through this low-pass filter. For fat, the spectrum is shifted to center the fat peak at $f = 0$, σ is recalculated, and the shifted FID is filtered to suppress water and retain fat. This procedure generates separate FID signals for water and fat.

Neuronal Firing Rate Estimation. Equations (4) and (5) were used to estimate neuronal firing fields from both water and fat FID signals. Equation (4) allows direct estimation of the unwrapped phase without a separate phase-unwrapping step. In the knee joint, FID T_2* ranges from 12–20 ms depending on coil location; beyond this, noise dominates. The 600–819 ms interval was used to estimate noise standard deviation, and the SNR was computed by dividing FID magnitude by this

value. Only segments with SNR > 10 were analyzed. Firing events were identified using peaks ≥1 ms wide, with a threshold of 0.3 × signal standard deviation and a minimum 1 ms separation. Firing rate (Hz) was computed as the number of peaks divided by the time window, separately for each coil and repetition. The median across 64 repetitions defined the final firing rate, reducing noise-induced errors. **Figures 2A - 2C** illustrate the full workflow, including spectral separation, signal processing, and firing rate computation.

Noise Sensitivity and Simulation. FR was first measured in a phantom containing 3%, 5%, and 7% agar gels and rubber (Figure 4M), which mimics T_2* properties of cartilage, meniscus, and tendon but lacks neurons. Ideally, FR should be zero; any detected signal reflects gradient or external noise. Each measurement was repeated three times. Noise effects were further evaluated using simulated FID signals (T_2* = 20 ms) perturbed by a neuronal firing field with six Gaussian peaks (σ = 0.1 ms), alternating polarity, and decreasing amplitudes. Noise levels were varied (SNR = 50–250), and the measured FR was compared to ground truth.

Outcome Measures

Association with OA status and $T_{1\rho}$. The cartilage and meniscus in the knee joint are divided into subregions (**Figure 3A**) based on their anatomical location (Medial-Lateral; Anterior-Posterior). The T1ρ values are estimated in the cartilage and meniscus of the knee joint using Mono-exponential fitting. Associations between FR measures (water & fat) and OA status were assessed at both participant and exploratory coil levels. For the participant-level analysis, FR was averaged across coil channels within the index knee, and the left and right knees were pooled for subsequent comparisons. Mean FR values were compared to healthy participants and patients with mild knee OA. Similarly, mean FR values were evaluated in relation to mean $T_{1\rho}$ for cartilage and meniscus. For exploratory spatial analyses, FR was evaluated separately for each coil channel and compared between healthy and OA groups. Left and right knees were evaluated separately because the spatial relationship between coil elements and anatomical cartilage and meniscal subregions differs by knee laterality. Channel-specific FR values were correlated with T1ρ values from individual cartilage and meniscal subregions. Analyses were conducted separately for water- and fat-compartment FID signals and for rest and ankle-flexion acquisitions.

Repeatability and Clinical Associations. In vivo FR repeatability was evaluated in three subjects with matched knee positioning, with FIDs acquired at rest and during ankle flexion and repeated

after 30 minutes. Agreement between FR across coil elements (K1–K15) was assessed between two acquisitions. For participant-level analyses, FR values were averaged across coils and repetitions within each participant's index knee, and the left and right knees were pooled. Associations between FR and the Western Ontario and McMaster Universities Osteoarthritis Index (WOMAC) total, pain, stiffness, and function scores were assessed to examine links between neuronal activity and pain, stiffness, and functional impairment.[40]

Statistical Analysis

Simulation accuracy was evaluated using the coefficient of determination (R^2), which quantifies the proportion of variance in observed data explained by the model, and the CV, which reflects relative variability in simulated outcomes. Measurement repeatability was assessed using Bland–Altman analysis to determine agreement between repeated measurements through mean differences and limits of agreement, alongside CV as a normalized measure of variability. Group differences in $T_{1\rho}$ and FR were analyzed using the Wilcoxon rank-sum test, with effect sizes (i.e., Cohen's d) reported to quantify group separation. Within-subject differences between rest and flexion conditions were evaluated using the Wilcoxon signed-rank test. Associations among FR, $T_{1\rho}$ relaxation times, and WOMAC scores were examined using Pearson correlation coefficients (r). Statistical significance was defined as $p < 0.05$.

Data Availability

The data supporting the findings of this study are not publicly available because they contain potentially identifiable human imaging data. De-identified data may be available from the corresponding author upon reasonable request and subject to institutional approval.

Code Availability

Custom code used for FID processing, water–fat separation, firing-rate estimation, and statistical analysis is available from the corresponding author upon reasonable request.

References

1. Abulhasan, J. & Grey, M. Anatomy and physiology of knee stability. *J. Funct. Morphol. Kinesiol.* **2**, 34 (2017).
2. Acar, H., Güngör, Y. & Bozkurt, M. Functional anatomy of the knee. *Clinical Anatomy of the Knee: An Atlas*. 1–57 (Springer, 2021).
3. Sakamoto, J. *et al.* Anatomical study of the articular branches innervating the hip and knee joint with reference to the mechanism of referral pain in patients with hip joint disease. *Clin. Anat.* **31**, 705-709. (2018).
4. Tran, J., Peng, P., Chan, V. & Agur, A. Overview of innervation of the knee joint. *Phys. Med. Rehabil. Clin. N. Am.* **32**, 767–778 (2021).
5. Suresh, R., Buddhiraju, A., Kuo, K., Dellon, A., Tuffaha, S. & Williams, E. A cadaveric study of the innervation of the anterior compartment of the knee. *Arch. Orthop. Trauma Surg.* **145**, 211 (2025).
6. Valls, J. O. *et al.* Anatomic and ultrasonographic evaluation of the knee sensory innervation: A cadaveric study to determine anatomic targets in the treatment of chronic knee pain. *Reg. Anesth. Pain Med.* **42**, 90–98 (2016).
7. Tran, J., Peng, P., Gofeld, M., Chan, V. & Agur, A. Anatomical study of the innervation of posterior knee joint capsule: Implication for image-guided intervention. *Reg. Anesth. Pain Med.* **44**, 234–238 (2019).
8. Yu, P., Loh, E., Agur, A. & Tran, J. Advanced three-dimensional anatomical mapping of saphenous and inferior medial genicular nerve branching: Enhancing precision in knee joint denervation. *Pain Med.* **26**, 8–13 (2024).
9. Coaccioli, S., Sarzi-Puttini, P., Zis, P., Rinonapoli, G. & Varrassi, G. Osteoarthritis: New insight on its pathophysiology. *J. Clin. Med.* **11**, 6013 (2022).
10. Li, Z., Huang, Z. & Bai, L. Cell interplay in osteoarthritis. *Front. Cell Dev. Biol.* **9**, 720477 (2021).
11. Semenistaja, S., Skuja, S., Kadiša, A. & Groma, V. Healthy and osteoarthritis-affected joints facing the cellular crosstalk. *Int. J. Mol. Sci.* **24**, 4120 (2023).
12. Chen, D. *et al.* Osteoarthritis: Toward a comprehensive understanding of pathological mechanism. *Bone Res.* **5**, 16044 (2017).
13. Paz-González, R. *et al.* An atlas of the knee joint proteins and their role in osteoarthritis defined by literature mining. *Mol. Cell. Proteomics* **22**, 100606 (2023).
14. Ozeki, N., Koga, H. & Sekiya, I. Degenerative meniscus in knee osteoarthritis: From pathology to treatment. *Life* **12**, 603 (2022).
15. Findlay, D. & Kuliwaba, J. Bone–cartilage crosstalk: A conversation for understanding osteoarthritis. *Bone Res.* **4**, 16028 (2016).

16. Schulze-Tanzil, G. Intraarticular ligament degeneration is interrelated with cartilage and bone destruction in osteoarthritis. *Cells* **8**, 990 (2019).
17. Yu, F. *et al.* Who drives the progress of osteoarthritis? A descriptive study of synovium-meniscus crosstalk. *Eur. Cell. Mater.* **48**, 93-114 (2024)
18. Chen, B. *et al.* Role of crosstalk between synovial cells and chondrocytes in osteoarthritis. *Exp. Ther. Med.* **27**, 70 (2024).
19. Zhou, S. *et al.* Source and hub of inflammation: The infrapatellar fat pad and its interactions with articular tissues during knee osteoarthritis. *J. Orthop. Res.* **40**, 1492–1504 (2022).
20. Malfait, A.M., Miller, R.E. & Miller, R.J. Basic mechanisms of pain in osteoarthritis: Experimental observations and new perspectives. *Rheum. Dis. Clin. North Am.* **47**, 165–180 (2021).
21. Zou, Y., Liu, C., Wang, Z., Li, G. & Xiao, J. Neural and immune roles in osteoarthritis pain: Mechanisms and intervention strategies. *J. Orthop. Translat.* **48**, 123–132 (2024).
22. Vasconcelos, D., Jabangwe, C., Lamghari, M. & Alves, C. The neuroimmune interplay in joint pain: The role of macrophages. *Front. Immunol.* **13**, 812962 (2022).
23. Kahraman, E. *et al.* Deciphering cartilage neuro-immune interactions and innervation profile through a 3D engineered osteoarthritic micropathophysiological system. *Mater. Today Bio* **31**, 101491 (2025).
24. Miller, R., Scanzello, C. & Malfait, A. An emerging role for Toll-like receptors at the neuroimmune interface in osteoarthritis. *Semin. Immunopathol.* **41**, 583–594 (2019).
25. Lockwood, S. M., Lopes, D. M., McMahon, S. B. & Dickenson, A. H. Characterisation of peripheral and central components of the rat monoiodoacetate model of osteoarthritis. *Osteoarthritis Cartilage* **27**, 712–722 (2019).
26. Morgan, M., Thai, J., Nazemian, V., Song, R. & Ivanusic, J. J. Changes to the activity and sensitivity of nerves innervating subchondral bone contribute to pain in late-stage osteoarthritis. *Pain* **163**, 390–402 (2022).
27. Vallbo, Å. B. Microneurography: How it started and how it works. *J. Neurophysiol.* **120**, 1415–1427 (2018).
28. Marino, M. & Mantini, D. Human brain imaging with high-density electroencephalography: Techniques and applications. *J. Physiol.* **604**, 783–812 (2026).
29. Akima, H., Tomita, A. & Ando, R. Effect of knee joint angle on the neuromuscular activation of the quadriceps femoris during repetitive fatiguing contractions. *J. Electromyogr. Kinesiol.* **49**, 102356 (2019).
30. Sakamoto, A., Khan, M. T. I. & Kurita, T. EMG signals in co-activations of lower limb muscles for knee joint analysis. In *2015 International Conference on Informatics, Electronics & Vision (ICIEV)* 1–5 (IEEE, 2015).
31. Qian, Y. *et al.* Quantum sensing MRI for noninvasive detection of neuronal electrical activity in human brains. *arXiv arXiv:2601.16423* (2026).

32. Eitner, A., Pester, J., Nietzsche, S., Hofmann, G. O. & Schaible, H.-G. The innervation of synovium of human osteoarthritic joints in comparison with normal rat and sheep synovium. *Osteoarthritis Cartilage* **21**, 1383–1391 (2013).
33. Zhu, S. *et al.* Subchondral bone osteoclasts induce sensory innervation and osteoarthritis pain. *J. Clin. Invest.* **129**, 1076–1093 (2019)
34. Fry, C. H. & Jabr, R. I. The action potential and nervous conduction. *Surgery* **28**, 49–54 (2010).
35. Pavelka, M. & Roth, J. Unmyelinated nerve fibre. In *Functional Ultrastructure* 322–323 (Springer, Vienna, 2010).
36. Havton, L. A. *et al.* Human organ donor-derived vagus nerve biopsies allow for well-preserved ultrastructure and high-resolution mapping of myelinated and unmyelinated fibers. *Sci. Rep.* **11**, 23831 (2021).
37. Krasnokutsky, S. *et al.* Quantitative magnetic resonance imaging evidence of synovial proliferation is associated with radiographic severity of knee osteoarthritis. *Arthritis Rheum.* **63**, 2983–2991 (2011).
38. Sharafi, A., Xia, D., Chang, G. & Regatte, R. R. Biexponential T1ρ relaxation mapping of human knee cartilage *in vivo* at 3 T. *NMR Biomed.* **30**, e3760 (2017).
39. Uecker, M. *et al.* ESPIRiT—an eigenvalue approach to autocalibrating parallel MRI: Where SENSE meets GRAPPA. *Magn. Reson. Med.* **71**, 990–1001 (2014).
40. Roos, E. M., Klassbo, M. & Lohmander, L. S. WOMAC osteoarthritis index: Reliability, validity, and responsiveness in patients with arthroscopically assessed osteoarthritis. *Scand. J. Rheumatol.* **28**, 210–215 (1999).

Acknowledgements

This study was supported by NIH grants R01-AR076328, R01-AR076985, and R01-AR078308. It was performed under the rubric of the Center of Advanced Imaging Innovation and Research (CAI^2R) at NYU Grossman School of Medicine, a NIBIB Biomedical Technology Resource Center (NIH P41 EB017183).

Author Contributions

Conceptualization: YQ, AM, RR. Methodology: YQ, AM, RR. Software: AM. Formal analysis: AM. Investigation: AM, HDM. Resources: YQ, JS, RR. Data curation: AM. Writing—original draft: AM. Writing—review and editing: AM, YQ, RR, HDM. Visualization: AM. Supervision: YQ, RR. Funding acquisition: RR. All authors approved the final manuscript.

Competing Interest

YQ is the inventor of U.S. Patent Application No. 63/467,482, titled *"Systems and methods for non-invasive detection of neuronal firings in humans via quantum-sensing magnetic resonance*

imaging," filed on May 18, 2023. The intellectual property is owned by New York University. All other authors (AM, HLM, JS, and RR) declare no conflicts of interest.

Figure Captions

Figure 1: (A) Schematic of action potential propagation along an axon, illustrating the generation of the associated neuronal magnetic field. (B) Temporal evolution of the action potential waveform, showing the dynamics of ion flow and its impact on the magnetic field signal. (C) Algorithmic workflow for estimating the neuronal firing field from FID signals, including phase extraction, peak detection, and computation of the corresponding firing rate (FR). This workflow captures both the temporal and spatial characteristics of neuronal activity from MR measurements.

Figure 2: Pipeline for estimating the MR signal–related field from multi-channel knee FID data (healthy subject example). Raw FIDs from individual coil elements (e.g., K1–K5) at the 32nd repetition are shown in the time domain with corresponding frequency spectra, revealing distinct water and fat components. Frequency-selective filtering isolates the water or fat spectral lobe, followed by an inverse Fourier transform to produce centered, band-limited FIDs with simplified mono-exponential decay and a single dominant spectral peak. The reconstructed signal field and detected peak occurrence rate are shown for the isolated water (B) and fat (C) FIDs. Dashed vertical lines indicate detected peaks using the following criteria: minimum peak distance = 1 ms, minimum peak width = 1 ms, and minimum peak height = 0.3 × the standard deviation of the signal field.

Figure 3: Knee joint segmentation and $T_{1\rho}$ mapping. (A) Anatomical subdivision into meniscus (Mn), patellar cartilage (PC), femoral cartilage (FC), and tibial cartilage (TC), further divided into anterior–posterior and medial–lateral subregions. (B) Representative $T_{1\rho}$ maps of left and right knees in a healthy control and an osteoarthritis (OA) patient. (C) Illustration of the rest and repeated ankle-flexion conditions during FID acquisition for estimation of the neuronal firing field and FR.

Figure 4: Agar gel phantom FID analysis across three repetitions. (A, E, I) FIDs from repetitions 1–3, respectively. (B, F, J) Corresponding magnitude spectra, and (C, G, K) neuronal firing fields derived from the FIDs. (D, H, L) Firing rates across channels (K1–K15) for each repetition. Peak detection used the following parameters: minimum peak distance = 1 ms, minimum peak width = 2 ms, and minimum peak height = 0.3 × the standard deviation of the neuronal firing field. (M) Schematic of the agar gel phantom used for the experiment.

Figure 5: Simulation framework for assessing the robustness of neuronal firing field estimation under noise. (A) A decaying FID (T_2^* = 20 ms) is modulated with a simulated neuronal firing field. Complex Gaussian noise is added across a range of SNR levels (50, 100, 150, and 250), and the neuronal firing field is re-estimated from the noisy FIDs. (B) Estimated neuronal firing field at SNR = 250. (C–F) Regression analysis comparing peak amplitudes between the ground-truth simulated firing field and the estimated field across different noise levels.

Figure 6: (A) illustrates the variation in $T_{1\rho}$ between the osteoarthritic cohort (OA) and healthy control (HS) for cartilage and meniscus. (B) illustrates the variation in water- and fat-signal FR between OA and HS at rest and repeated ankle flexion. (C) illustrates the variation in water- and

fat-signal FR with cartilage and meniscus T1ρ at rest and repeated ankle flexion. Median $T_{1\rho}$ values are estimated across all subregions of cartilage and meniscus. Mean FR is estimated across all channels.

Figure 7: Linear regression analysis of firing rate (FR) and WOMAC scores. Panels (A)–(D) show the relationships between water-derived FR and total WOMAC score (A), stiffness (B), pain (C), and function (daily activities) (D). Panels (E)–(H) show the corresponding relationships for fat-derived FR versus total WOMAC score (E), stiffness (F), pain (G), and function (H).

Figure 8: Repeatability of firing rate (FR) measurements from water and fat FIDs in three healthy subjects. (A) Schematic of FID acquisition at rest and during ankle flexion. (B–C) Bland–Altman plots for FR derived from water FID at rest (B) and flexion (C), showing agreement across repeated measurements. (D) Coefficient of variation (CV) of water-derived FR across individual coil elements for rest and flexion. (E–F) Bland–Altman plots for FR derived from fat FID at rest (E) and flexion (F). (G) CV of fat-derived FR across individual coil elements for both conditions.

Tables

Table 1: Firing rate (FR) values for healthy subjects (HS) and osteoarthritis (OA) patients in the left and right knees, measured under rest and ankle flexion conditions**.** p-values (p) and effect sizes (d) were calculated to assess differences between the HS and OA groups.

Coil	FID Compartment	Left								Right							
		rest				Flexion				rest				Flexion			
		HS	OA	p	d	HS	OA	p	d	HS	OA	p	d	HS	OA	p	d
K1	Water	65.36 [56.9-75.9]	51.94 [51.8-65.5]	0.4	-0.72	51.94 [51.8-65.5]	51.87 [50.0-71.0]	0.7	-0.51	63.11 [57.7-67.5]	77.05 [55.9-112.9]	0.63	0.85	77.05 [55.9-112.9]	61.94 [57.6-84.6]	1	-0.32
	Fat	87.34 [82.1-93.1]	97.79 [89.6-101.6]	0.4	1.05	**87.3 [82.6-98.7]**	**110.8 [104.6-118.5]**	**0.07**	**1.45**	112.31 [103.2-144.5]	136.59 [102.9-153.0]	1	0.16	**100.8 [99.1-131.4]**	**154.7 [118.8-178.6]**	**0.07**	**1.01**
K2	Water	64.86 [44.5-83.0]	46.26 [42.6-66.9]	1	-0.46	46.26 [42.6-66.9]	52.28 [48.3-71.6]	1	0.152	65.62 [60.1-73.0]	87.70 [76.8-109.2]	0.11	1.61	87.70 [76.8-109.2]	79.98 [69.0-102.0]	0.4	-0.82
	Fat	**85.2 [81.2-85.4]**	**128.3 [116.2-140.1]**	**0.03**	**2.39**	**93.1 [80.7-95.8]**	**120.8 [104.7-153.5]**	**0.07**	**1.63**	103.92 [99.5-138.2]	118.08 [109.3-129.2]	0.4	0.01	118.08 [109.3-129.2]	132.98 [130.8-135.5]	0.4	0.39
K3	Water	64.13 [58.1-103.3]	50.06 [48.7-90.4]	0.4	-0.36	50.06 [48.7-90.4]	66.15 [62.2-93.5]	1	0.124	89.89 [67.4-94.6]	57.04 [56.9-80.7]	0.63	-0.65	**66.5 [63.8-73]**	**93.7 [92.3-101.7]**	**0.01**	**4.41**
	Fat	97.42 [95.5-110.1]	143.65 [86.2-159.6]	0.7	0.62	143.65 [86.2-159.6]	147.77 [105.5-154.3]	0.7	1.504	**88.5 [72.5-106.7]**	**140.9 [127.0-156.7]**	**0.02**	**2.02**	**99.1 [88.2-107.7]**	**128.2 [108.9-145.7]**	**0.04**	**1.39**
K4	Water	**125.2 [102.7-132.6]**	**89.2 [80.5-96]**	**0.07**	**-1.67**	93.11 [88.3-94.1]	75.69 [68.0-110.8]	0.7	-0.74	82.80 [69.7-106.6]	90.01 [75.3-97.0]	1	-0.07	90.01 [75.3-97.0]	71.75 [67.0-99.0]	0.4	0.57
	Fat	97.51 [87.1-108.3]	129.55 [94.4-147.5]	0.7	0.89	129.55 [94.4-147.5]	127.09 [89.2-128.6]	0.7	-0.739	83.91 [83.3-98.5]	133.95 [105.1-154.1]	0.11	1.66	133.95 [105.1-154.1]	124.28 [101.6-153.1]	0.4	1.04
K5	Water	84.52 [84.0-96.6]	86.61 [73.6-130.1]	1	0.37	86.61 [73.6-130.1]	66.29 [62.3-117.9]	0.7	-0.323	81.02 [67.1-92.5]	88.39 [58.2-91.4]	0.86	0.17	88.39 [58.2-91.4]	70.11 [69.3-71.2]	0.4	0.77
	Fat	91.11 [79.8-100.6]	129.54 [80.6-152.4]	0.7	0.77	129.54 [80.6-152.4]	133.24 [90.4-138.8]	0.7	0.699	**110.12 [100.2-117.7]**	**171.64 [131.0-180.2]**	**0.02**	**1.94**	171.64 [131.0-180.2]	148.50 [115.6-179.1]	0.23	1.66
K6	Water	**79.9 [71.2-81.2]**	**56.1 [50.8-58.1]**	**0.04**	**-3.87**	**67.3 [58-77.6]**	**51.2 [47.2-56.2]**	**0.07**	**-1.83**	56.44 [48.8-61.8]	50.76 [29.5-68.9]	0.86	-0.33	50.76 [29.5-68.9]	57.95 [33.0-63.0]	0.63	0.31
	Fat	102.05 [92.1-114.1]	90.99 [88.1-121.0]	1	-0.003	90.99 [88.1-121.0]	106.50 [104.0-135.3]	0.7	0.83	105.52 [102.1-144.1]	108.80 [102.0-127.6]	1	0.28	108.80 [102.0-127.6]	136.99 [128.1-163.8]	0.63	0.38
K7	Water	**82.6 [80.3-82.7]**	**56.3 [51.5-69.2]**	**0.04**	**-2.26**	55.49 [48.2-73.3]	49.20 [42.8-72.0]	0.7	-1.40	46.09 [43.8-50.7]	57.21 [40.8-81.5]	0.63	0.76	57.21 [40.8-81.5]	60.11 [47.3-75.0]	0.63	0.56
	Fat	99.16 [93.5-137.6]	102.11 [100.9-104.7]	0.7	0.48	102.11 [100.9-104.7]	107.60 [99.3-119.9]	0.7	0.36	109.06 [93.9-140.4]	107.96 [91.9-131.4]	0.86	0.20	107.96 [91.9-131.4]	127.20 [120.9-134.0]	0.63	0.39
K8	Water	70.89 [67.9-82.9]	55.69 [54.4-83.2]	0.7	0.44	55.69 [54.4-83.2]	61.98 [43.4-82.2]	0.7	-0.27	58.75 [52.3-63.6]	71.95 [57.0-78.2]	0.4	0.93	71.95 [57.0-78.2]	48.09 [46.7-69.9]	0.63	-0.22

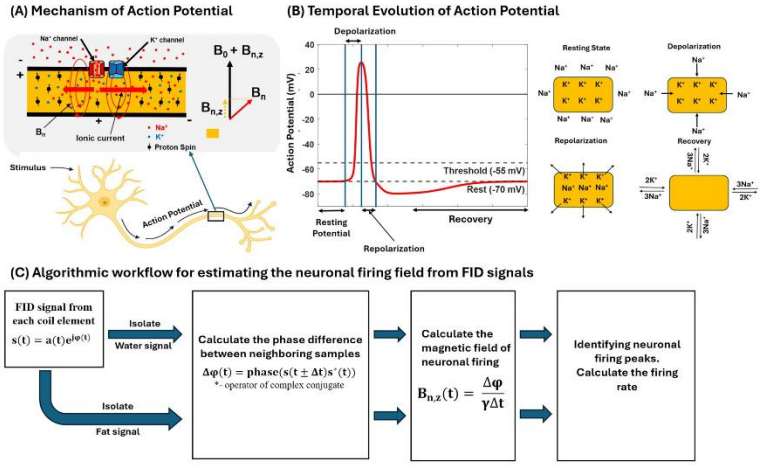
	Fat	93.50 [85.1-127.7]	124.50 [111.1-124.9]	0.7	-0.61	124.50 [111.1-124.9]	127.15 [101.4-136.0]	0.4	0.75	123.25 [101.0-144.2]	129.48 [125.1-131.7]	1	0.30	129.48 [125.1-131.7]	136.28 [132.5-136.3]	0.11	1.65
K9	Water	75.51 [58.8-81.7]	59.75 [53.8-65.9]	0.4	0.88	59.75 [53.8-65.9]	47.01 [46.5-68.3]	0.7	-0.62	48.87 [39.9-62.5]	46.98 [41.6-62.1]	1	-0.01	46.98 [41.6-62.1]	46.60 [43.7-57.9]	0.63	-0.30
	Fat	108.93 [78.6-118.4]	122.71 [99.9-123.0]	0.4	-0.56	122.71 [99.9-123.0]	127.07 [106.0-131.4]	0.4	1.44	122.74 [102.4-148.7]	137.20 [136.8-140.3]	0.86	0.58	137.20 [136.8-140.3]	154.14 [141.9-169.6]	0.23	1.48
K10	Water	**67.78 [64.7-72.7]**	**44.89 [41.1-55.1]**	**0.07**	**2.67**	**66 [60.6-68]**	**48.2 [44.7-58.9]**	**0.07**	**-1.77**	53.69 [52.1-57.1]	68.49 [57.3-69.0]	0.4	1.42	68.49 [57.3-69.0]	56.27 [51.6-65.7]	0.63	-0.92
	Fat	**91.97 [87.1-103.1]**	**122.9 [102.4-131.7]**	**0.07**	**-1.58**	119.00 [93.6-124.9]	112.45 [106.8-128.6]	0.4	-1.21	148.77 [98.6-192.5]	120.41 [106.6-125.6]	0.86	0.67	120.41 [106.6-125.6]	154.35 [127.9-156.7]	1	0.13
K11	Water	69.50 [57.8-80.7]	61.46 [59.8-77.5]	1	0.10	61.46 [59.8-77.5]	70.43 [60.1-98.8]	1	0.34	73.70 [70.2-81.9]	72.14 [72.1-75.6]	0.86	0.36	72.14 [72.1-75.6]	62.09 [41.3-80.3]	0.86	-0.37
	Fat	**91.41 [89.7-100.3]**	**150.3 [105.5-159.3]**	**0.04**	**-2.35**	**94.5 [93.7-100.7]**	**146.1 [141-165.8]**	**0.04**	**4.22**	126.89 [88.8-164.7]	127.98 [108.5-173.4]	0.63	0.29	127.98 [108.5-173.4]	128.10 [110.3-147.0]	0.86	0.24
K12	Water	66.92 [63.5-72.2]	71.61 [67.7-92.9]	0.7	-0.86	71.61 [67.7-92.9]	81.05 [78.2-104.5]	0.4	1.42	62.76 [57.1-66.3]	70.89 [67.8-89.8]	0.11	1.42	70.89 [67.8-89.8]	71.52 [45.6-82.0]	0.63	0.26
	Fat	86.36 [82.8-95.1]	99.01 [92.5-124.1]	0.2	-1.11	**99.01 [92.5-124.1]**	**135.8 [126.7-146.8]**	**0.07**	**2.23**	131.02 [98.7-160.6]	140.86 [130.7-161.6]	0.63	0.51	140.86 [130.7-161.6]	124.61 [116.9-142.4]	0.86	0.24
K13	Water	86.32 [81.7-121.4]	67.15 [55.3-105.2]	0.4	0.66	67.15 [55.3-105.2]	81.04 [74.4-103.4]	0.7	0.44	67.80 [54.3-84.7]	66.26 [60.9-96.6]	0.63	0.37	66.26 [60.9-96.6]	59.45 [52.0-96.3]	0.86	0.08
	Fat	100.43 [78.0-106.1]	96.79 [96.8-111.6]	1	-0.64	**96.79 [96.8-111.6]**	**136.8 [125.9-157.7]**	**0.07**	**2.21**	116.96 [99.8-138.5]	140.47 [129.9-147.1]	0.4	1.03	140.47 [129.9-147.1]	161.89 [130.6-173.0]	0.23	1.11
K14	Water	74.06 [70.5-79.8]	71.13 [66.4-82.8]	1	0.09	71.13 [66.4-82.8]	77.36 [71.2-81.5]	0.2	1.38	70.88 [66.2-82.9]	63.30 [58.4-89.8]	0.63	-0.09	63.30 [58.4-89.8]	55.30 [47.6-91.7]	0.63	-0.33
	Fat	**98.11 [85.8-105.5]**	**131.45 [106.0-157.8]**	**0.07**	**-1.61**	**95.2 [78.6-101.8]**	**116.3 [103.6-163.9]**	**0.07**	**1.63**	125.77 [112.7-144.1]	153.60 [118.1-162.0]	0.63	0.53	153.60 [118.1-162.0]	172.43 [126.7-177.4]	0.23	1.04
K15	Water	**76.8 [76-89.1]**	**55.6 [41.9-67.3]**	**0.04**	**1.67**	65.10 [33.3-71.6]	62.90 [60.0-91.8]	0.7	-0.51	69.86 [56.6-83.5]	70.42 [69.4-93.8]	0.63	0.61	70.42 [69.4-93.8]	67.85 [52.6-91.0]	0.86	-0.16
	Fat	111.48 [94.9-111.6]	106.16 [89.6-187.7]	1	-0.61	**103.5 [95.1-107.3]**	**125.2 [115.1-159]**	**0.04**	**4.22**	143.59 [125.9-161.5]	158.30 [131.8-171.3]	0.63	0.37	158.30 [131.8-171.3]	159.25 [135.8-169.4]	0.63	0.63

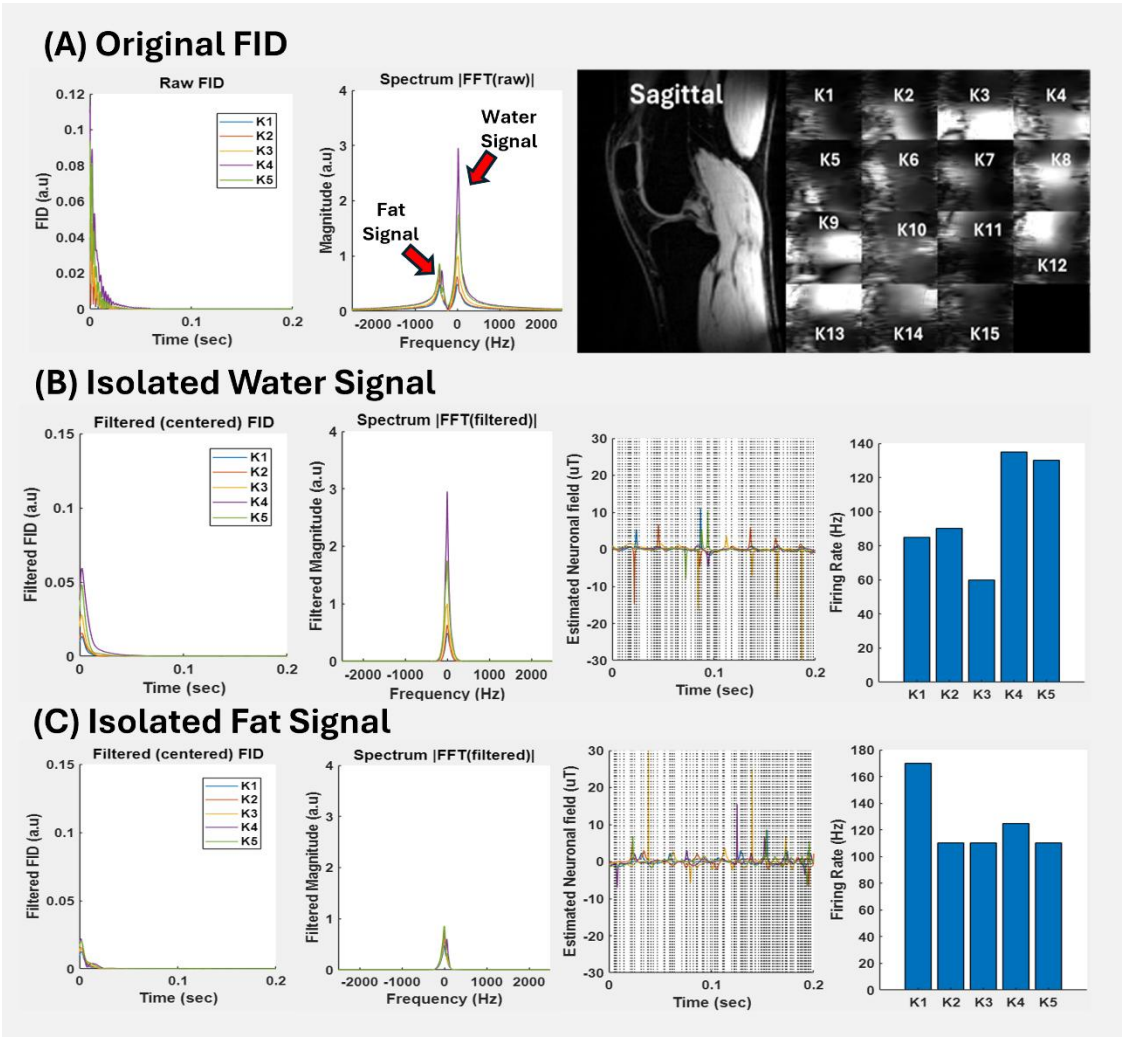
p: p-value, d: Effect Size, **HS:** healthy volunteer, **OA:** subject with osteoarthritis.

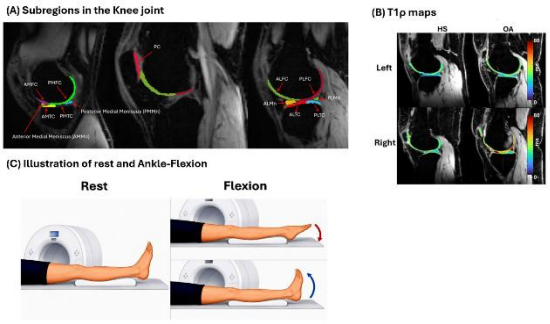
Table 2: Sequence parameters for the FID acquisition used to measure neuronal firing and for the $T_{1\rho}$-weighted imaging sequences.

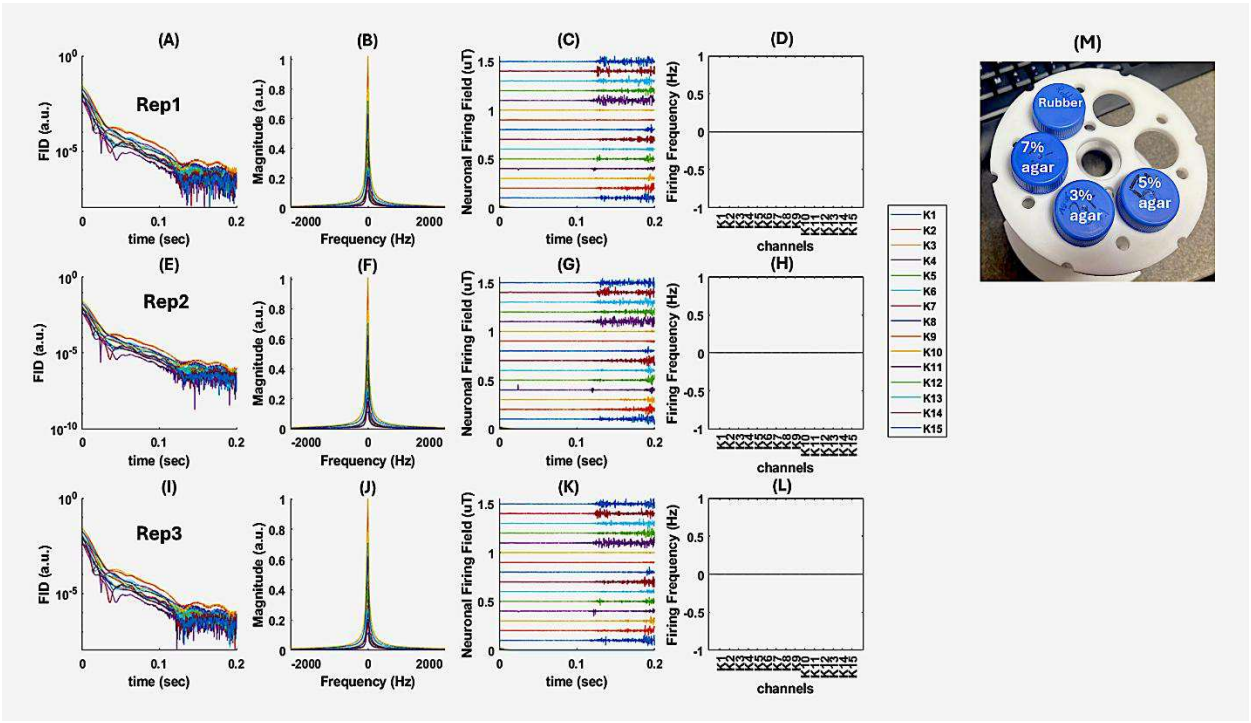
Parameter	FID Parameters	$T_{1\rho}$ Weighted images
FOV	-	160 mm
Base Resolution	-	192
Slices per Slab	-	36
Vector Size	2048	
Number of Slabs	-	1
Voxel Size	-	0.8 mm x 0.8 mm x 3mm
TR	1500 ms	1500 ms
TE	0.2 ms	5.22 ms
Pulse Duration	0.2 ms	-
Echo Spacing	-	8.9 ms
Bandwidth	2500 Hz	490Hz/Px
Turbo Factor	-	64
Number of Shots	-	128
Number of Average	64	-
Acquisition Duration/ Echo	819 ms	
Spin Lock Frequency	-	500Hz
Spin Lock Duration	-	0.5, 3.8, 9.8, 21.8 ms
Duration	1 min 36 seconds	1 min 29 second/TSL

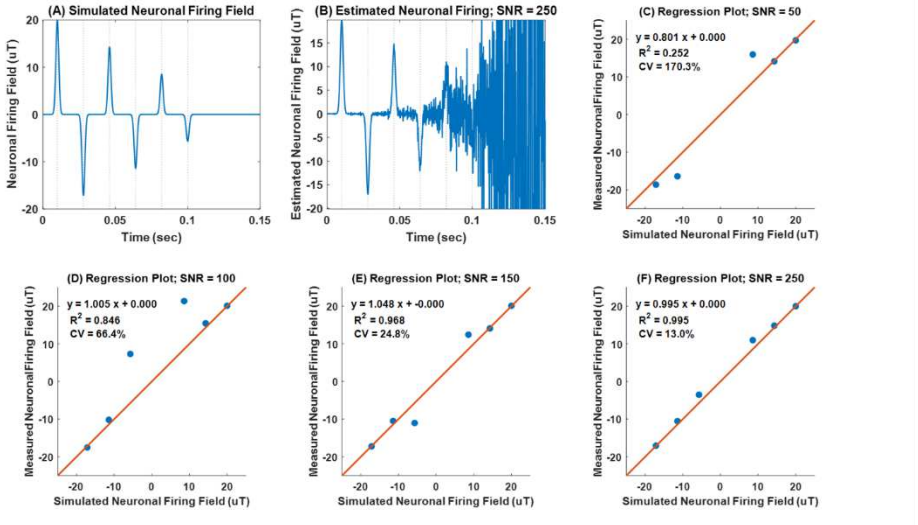
Figures


(A) Mechanism of Action Potential
(B) Temporal Evolution of Action Potential
Depolarization
Threshold (-55 mV)
Rest (-70 mV)
Resting Potential
Repolarization
Recovery
Resting State
Repolarization
Depolarization
Recovery
Stimulus
Action Potential
Ionic current
Proton Spin
(C) Algorithmic workflow for estimating the neuronal firing field from FID signals
FID signal from each coil element
$s(t) = a(t)e^{i\varphi(t)}$
Isolate Water signal
Isolate Fat signal
Calculate the phase difference between neighboring samples
$\Delta\varphi(t) = \mathbf{phase}(s(t \pm \Delta t)s^*(t))$
*- operator of complex conjugate
Calculate the magnetic field of neuronal firing
$B_{n,z}(t) = \frac{\Delta\varphi}{\gamma\Delta t}$
Identifying neuronal firing peaks. Calculate the firing rate

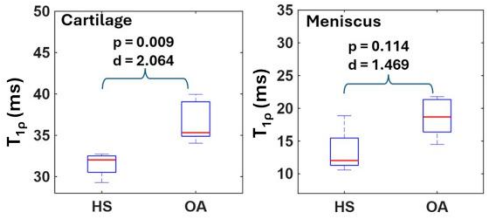

(A) Original FID
Raw FID
FID (a.u)
Time (sec)
K1
K2
K3
K4
K5
Spectrum |FFT(raw)|
Water Signal
Fat Signal
Magnitude (a.u)
Frequency (Hz)
Sagittal
K1
K2
K3
K4
K5
K6
K7
K8
K9
K10
K11
K12
K13
K14
K15
(B) Isolated Water Signal
Filtered (centered) FID
Filtered FID (a.u)
Time (sec)
Spectrum |FFT(filtered)|
Filtered Magnitude (a.u)
Frequency (Hz)
Estimated Neuronal field (uT)
Time (sec)
Firing Rate (Hz)
K1
K2
K3
K4
K5
(C) Isolated Fat Signal
Filtered (centered) FID
Filtered FID (a.u)
Time (sec)
Spectrum |FFT(filtered)|
Filtered Magnitude (a.u)
Frequency (Hz)
Estimated Neuronal field (uT)
Time (sec)
Firing Rate (Hz)
K1
K2
K3
K4
K5


(A) Subregions in the Knee joint
(B) T1ρ maps
HS
OA
Left
Right
(C) Illustration of rest and Ankle-Flexion
Rest
Flexion

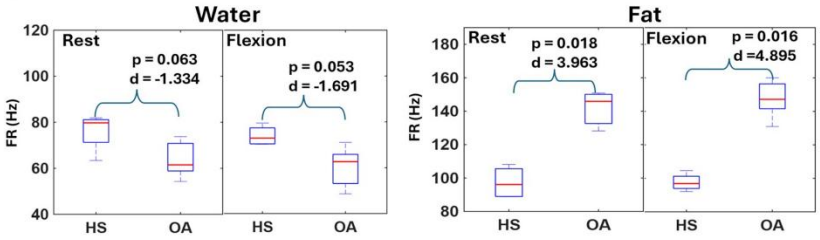

(A)
(B)
(C)
(D)
Rep1
FID (a.u.)
Magnitude (a.u.)
Neuronal Firing Field (uT)
Firing Frequency (Hz)
time (sec)
Frequency (Hz)
channels
(E)
(F)
(G)
(H)
Rep2
(I)
(J)
(K)
(L)
Rep3
K1
K2
K3
K4
K5
K6
K7
K8
K9
K10
K11
K12
K13
K14
K15
(M)
Rubber
7% agar
3% agar
5% agar


(A) Simulated Neuronal Firing Field
(B) Estimated Neuronal Firing; SNR = 250
(C) Regression Plot; SNR = 50
Neuronal Firing Field (uT)
Estimated Neuronal Firing Field (uT)
Measured NeuronalFiring Field (uT)
Time (sec)
Simulated Neuronal Firing Field (uT)
y = 0.801 x + 0.000
R2 = 0.252
CV = 170.3%
(D) Regression Plot; SNR = 100
y = 1.005 x + 0.000
R2 = 0.846
CV = 66.4%
(E) Regression Plot; SNR = 150
y = 1.048 x + -0.000
R2 = 0.968
CV = 24.8%
(F) Regression Plot; SNR = 250
y = 0.995 x + 0.000
R2 = 0.995
CV = 13.0%

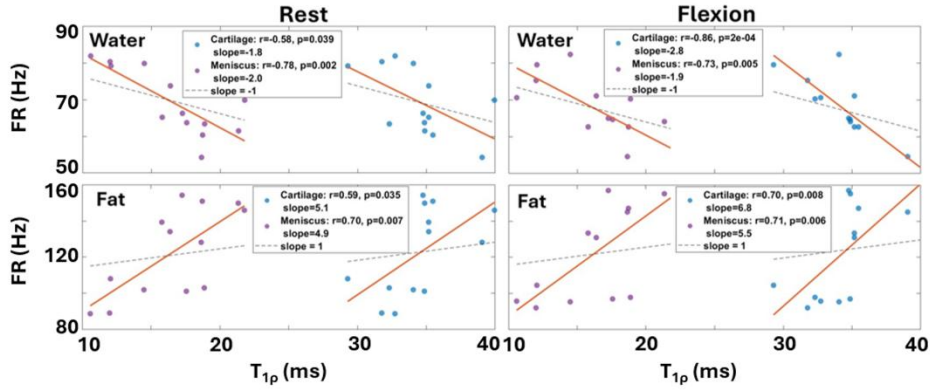
(A) T1ρ (OA vs HS)

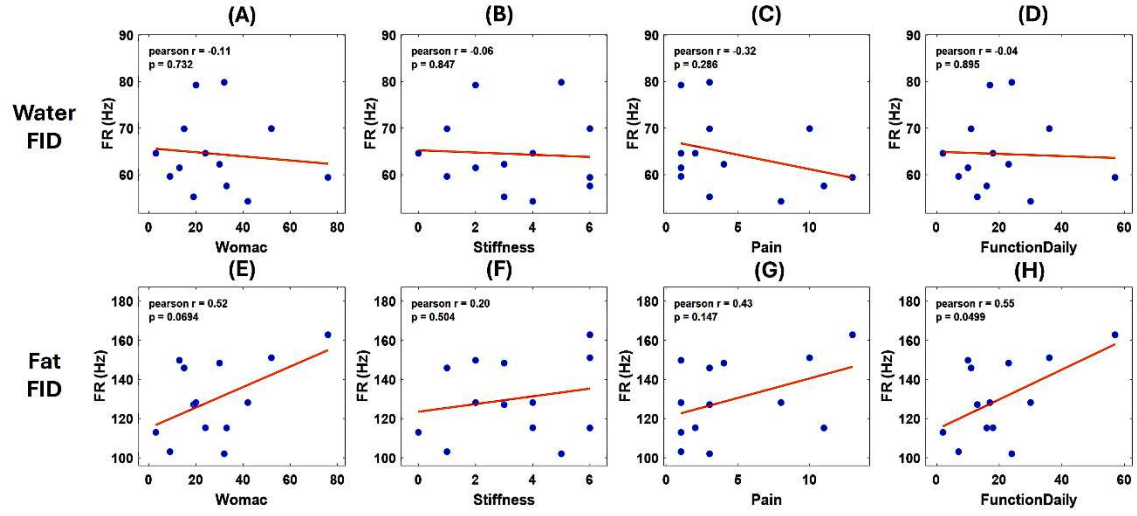


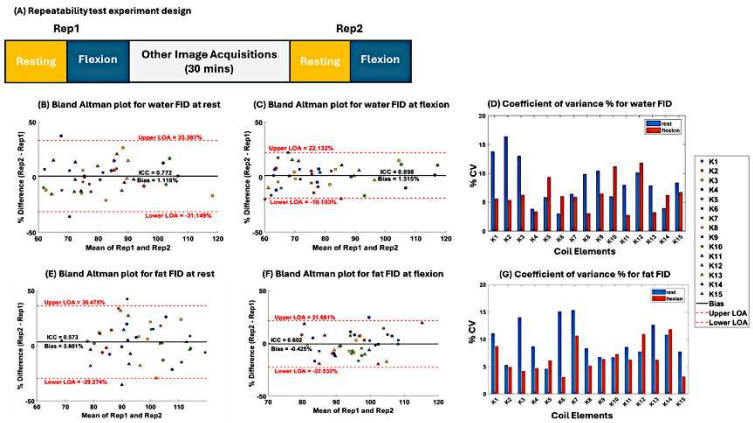
(B) Firing rate (OA vs HS)



(C) Correlation between Firing rate and T1ρ






(A) Repeatability test experiment design
Rep1
Rep2
Resting
Flexion
Other Image Acquisitions (30 mins)
Resting
Flexion
(B) Bland Altman plot for water FID at rest
Upper LOA = 23.381%
ICC = 0.772
Bias = 1.119%
Lower LOA = -31.145%
% Difference (Rep2 - Rep1)
Mean of Rep1 and Rep2
(C) Bland Altman plot for water FID at flexion
Upper LOA = 22.132%
ICC = 0.898
Bias = 1.513%
Lower LOA = -19.103%
% Difference (Rep2 - Rep1)
Mean of Rep1 and Rep2
(D) Coefficient of variance % for water FID
rest
flexion
% CV
Coil Elements
K1
K2
K3
K4
K5
K6
K7
K8
K9
K10
K11
K12
K13
K14
K15
Bias
Upper LOA
Lower LOA
(E) Bland Altman plot for fat FID at rest
Upper LOA = 36.473%
ICC = 0.573
Bias = 3.601%
Lower LOA = -29.274%
% Difference (Rep2 - Rep1)
Mean of Rep1 and Rep2
(F) Bland Altman plot for fat FID at flexion
Upper LOA = 21.681%
ICC = 0.662
Bias = -0.425%
Lower LOA = -22.532%
% Difference (Rep2 - Rep1)
Mean of Rep1 and Rep2
(G) Coefficient of variance % for fat FID
rest
flexion
% CV
Coil Elements

Supplementary Files

This is a list of supplementary files associated with this preprint. Click to download.

- QSnatureSRSupplementaryMaterial.docx